Spatial Element Distribution Control in a Fully Solution-Processed Nanocrystals-Based 8.6% Cu$_2$ZnSn(S,Se)$_4$ Device

Wan-Ching Hsu,[+] Huanping Zhou,[+,]* Song Luo, Tze-Bin Song, Yao-Tsung Hsieh, Hsin-Sheng Duan, Shenglin Ye, Wenbing Yang, Chia-Jung Hsu, Chengyang Jiang, Brion Bob, and Yang Yang*

Department of Materials Science and Engineering, University of California, Los Angeles, California 90095, United States. [+]These authors contributed equally to this work.

ABSTRACT A fully solution-processed high performance Cu$_2$ZnSn(S,Se)$_4$ (CZTSSe, kesterite) device has been demonstrated. It is based on the rational engineering of elemental spatial distributions in the bulk and particularly near the surface of the film from nanocrystal precursors. The nanocrystals are synthesized through a modified colloidal approach, with excellent solubility over a large compositional window, followed by a selenization process to form the absorber.

Cu$_2$ZnSn(S,Se)$_4$ Photovoltaics
Metal · Se · Element re-distribution · 8.6% · Full solution process

The X-ray photoluminescence (XPS) depth profiling indicates an undesirable Sn-rich surface of the selenized film. An excessive Zn species was quantitatively introduced through nanocrystals precursor to correct the element distribution, and accordingly a positive correlation between the spatial composition in the bulk/surface film and the resulting device parameter is established. The enhanced device performance is associated with the reduced interfacial recombination. With a Zn content 1.6 times more than the stoichiometry; the optimized device, which is fabricated by employing a full solution process from the absorber to the transparent top electrode, demonstrates a performance of 8.6%. This composition-control approach through stoichiometric adjustments of nanocrystal precursors, and the developed correlation between the spatial composition and device performance may also benefit other multielement-based photovoltaics.
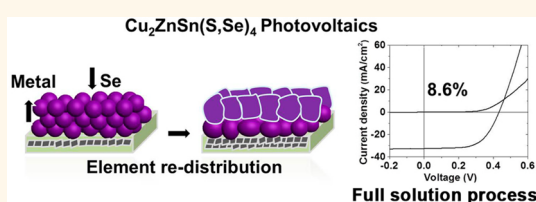
KEYWORDS: Cu$_2$ZnSn(S,Se)$_4$ · spatial composition · nanocrystals · solution process · photovoltaics

The use of earth-abundant materials on solar cells eases the natural resource restriction on the energy production capacity, which is necessary to fulfill the growing energy demand.[1] Kesterite (Cu$_2$ZnSn(S,Se)$_4$, CZTSSe), composed of earth-abundant elements,[2] is a thin-film solar-cell absorber material, which currently reaches 7% to 12.6% power conversion efficiencies in lab-scale based on a variety of vapor-phase and liquid-phase processes.[3−6] It is well recognized that, rooted in the quaternary nature of the material, the key challenges for CZTS solar cells is sophisticated phase and composition control, avoiding apparent detrimental secondary phases,[7−12] and harmful point defects, which are dependent on the chemical potential environment, that is, composition.[13−15] In the effort to fabricate high performance CZTSSe solar cells, a composition that is Zn-rich, Cu-poor, and Sn-poor compared to the stoichiometric

composition of kesterite Cu$_2$ZnSn(S,Se)$_4$ is identified in most studies.[3−6,16] However, an accurate control of the bulk composition does not guarantee uniform spatial distribution of the elements throughout the film. These localized nonideal chemical potentials may produce unfavorable point defects, which serve as recombination centers.[14,17,18] In this regard, it is crucial to understand the processing-dependent spatial elemental distributions, including the lateral and vertical distribution, and more importantly, a rational correlation between the device performance and the special element distribution is urgently needed to further advance the CZTSSe devices.

As a promising solution processing method, Cu$_2$ZnSnS$_4$(CZTS) nanocrystal-based deposition[19−23] utilizes the controlled synthesis of nanocrystals to produce nanocrystal inks with prescribed material properties. It provides a unique chemical tool to control

composition and phase prior to film formation in the liquid state owing to the large solution-state diffusivity values of the synthetic precursors, which allows the nanoparticles to reach thermodynamically stable phases with highly uniform composition distributions. However, the transformation from nanosized to microsized grains via this process requires the film to be annealed at a high temperature (around 500 °C) in the presence of selenium vapor, often described as a "selenization process". Such a selenization process induces the nucleation and growth of a layer of large CZTSSe grains on the surface of the nanocrystal films, resulting in a bilayered structure (e.g., separate large grain and fine grain layers). Since the large grains are primarily responsible for the generation of photocurrent, intuitively, the spatial composition of the newly formed large grains rather than initial bulk composition determines the device performance. Moreover, vigorous vertical atomic diffusion processes including the up-diffusion of metal ions and the downward diffusion/substitution of Se over S are involved in the nucleation and growth of the new large grains, it is of interest to understand the composition uniformity of metal ratios and S/Se ratios vertically and laterally. In previous studies, composition depth profiling has shown that the compositions are relatively ununiform for the films prepared by this particular process.[22] However, generally for all processes, there is lack of insight into how the spatial composition of the selenized film may be correlated to device performance, other than the understanding that a Zn-rich, Cu-poor, Sn-poor bulk composition produces higher device performance. In addition, multiple studies, not limited to certain processes, have consistently shown evidence of dominant interfacial recombination.[24,25] Thus, it is particularly interesting to understand the local composition in the vicinity of the junction, that is, the surface composition of the selenized film and the related device performance, which is crucial to alleviate the dominant interfacial recombination, and eventually benefit CZTSSe devices.

Herein, we demonstrate a fully solution-processed high performance CZTSSe device based on the rational engineering of elemental spatial distributions in the bulk and particularly surface film upon intentional stoichiometry compensation in nanocrystals. A modified colloidal method was employed to synthesize nanocrystals, providing excellent nanoparticle solubility over a large compositional window. The spatial composition distribution in the selenized film was analyzed by X-ray photoluminescence (XPS) depth profiling, which indicated a nonuniform distribution of metals from the front to the back of absorber layer. Interestingly, composition gradient near the film surface shows an undesirable Sn-rich surface, which may associate with the low surface energy of the corresponding point defects. Through the introduction of high Zn content into the precursors, the Sn-rich surface composition in the film is partially corrected. A correlation between the spatial composition in the bulk/surface film and the resulting device parameter points out that an increased Zn/Sn ratio in the film surface helps to suppress the interfacial recombination in the devices, and improves the device performance. By choosing a bulk composition with a higher Zn ratio compared to the commonly chosen composition, we successfully alter the surface composition and demonstrate a better cell efficiency. The best cell efficiency is 8.6%, which is fabricated by employing a full solution process from the absorber to the transparent top electrode. Furthermore, we indicate the challenges of S/Se grain-to-grain ratio variation and vertical gradient, which could be also relevant for device performance.

RESULTS AND DISCUSSION

To investigate how various initial compositions change after undergoing the vigorous vertical diffusion process during selenization, we first explored the synthesis of CZTS nanocrystals to gain a wider window of composition without sacrificing dispersibility in organic solvent. Synthetic details are provided in the experimental section, following a reported colloidal synthesis procedure[26] with some modification. In brief, CZTS nanocrystals were prepared by injecting sulfur dissolved in oleylamine solution into a mixture of $Cu(acac)_2$, $Zn(acac)_2$, and $Sn(acac)_2Cl_2$ in oleylamine at 225 °C, and reacting for 1 h. Structural characterization of the CZTS nanocrystals was performed with X-ray diffraction (XRD) (Figure 1a) and transmission electron microscopy (TEM) (Figure 1b). The characteristic XRD peaks of kesterite CZTS from the (112), (200), (220), (312), and (008) planes are visible in the diffraction spectrum (JCPDS 00-026-0575). According to the Scherrer equation, the calculated crystal size of the CZTS nanoparticles is 10.8 nm. TEM images presented in Figure 1b further indicate the highly crystalline nature of CZTS nanocrystals and that the typical particle size is between 10 and 15 nm, accompanied with a small fraction of small-sized particles. The characteristic interplanar distance of 0.32 nm from a (112) plane of kesterite is also shown in a typical HRTEM image (Figure 1b inset).

The effective incorporation of specific ions into the quaternary CZTS nanocrystals relies on the balance between precursor dissociation and nanoparticle growth kinetics. Also, the solubility of nanocrystals is determined by the dissociation capability of the precursors and coordination ability between surfactants and specific surface atoms.[14,27] In the present work, $Sn(acac)_2Cl_2$ was used as the Sn precursor to replace previously reported $Sn(acac)_2Br_2$,[26] owing to the relatively stronger electronegativity of Cl, which may destabilize the Sn precursor and facilitate decomposition. A wide composition window in the as-prepared CZTS nanocrystals (e.g., Cu/Sn ranging from 1.5 to 2.0, and
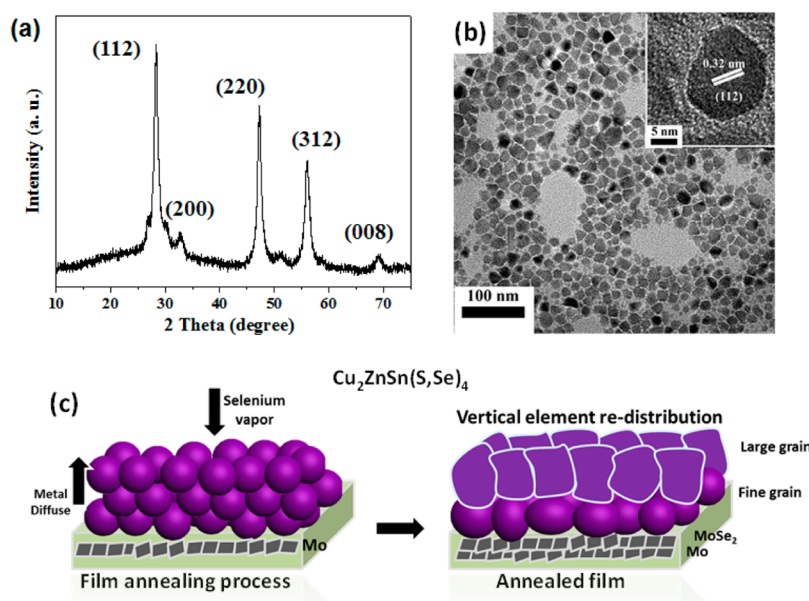
Figure 1. As-prepared CZTS nanocrystals: (a) XRD pattern; (b) TEM and HRTEM images; (c) schematic illustration of film annealing process based on selenium vapor diffusion into the film, and the upward diffusion of metals.

Zn/(Cu+Zn+Sn) ranging from 28% to 40%) has thus been achieved. All CZTS nanocrystals with a fixed Cu/Sn value and a variety of Zn/(Cu+Zn+Sn) values exhibit good solubility in nonpolar solvents, albeit slightly different particle sizes (shown in Supporting Information, Figure S1). Additionally, the nanocrystals self-assemble into partially ordered micrometer-scale patterns, suggesting effective surface passivation by ligands (Figure S2). As a comparison, when $Sn(acac)_2Br_2$ as Sn is used as a precursor, the nanocrystals with composition of Cu/Sn = 1.76, and Zn/(Cu+Zn+Sn) = 0.39, exhibit decreased dispersibility in solvent, due to the formation of apparently large-sized crystals (Figure S3). Hence, using $Sn(acac)_2Cl_2$ as Sn source ensures both composition tunability over a large stoichiometry range and sufficient solubility in nonpolar solvents.

Next, we assembled the preformed CZTS nanocrystals into films, followed by post-selenization. Film deposition was achieved through multiple spin coatings of the CZTS nanocrystal dispersion onto Mo-coated glass substrates, while selenization was carried out at 560 °C for 20 min, in argon atmosphere slightly above 1 atm. Fabrication details are shown in the experimental section. As visible in the scanning electron microscope (SEM) image shown in Supporting Information, Figure S4, the films exhibit a layered structure composed of large grains of CZTSSe, fine grains of carbon-rich CZTSSe, and $MoSe_2$/Mo phases at the back contact. The formation of a carbon-rich CZTSSe layer is likely due to the existence of organic capping agents which are chemically bound to the surface of the nanoparticles trapped within the film prior to annealing.[28,29] The composition depth profiles in the selenized film was characterized via X-ray photoelectron spectroscopy (XPS) depth profiling, in which Ar sputtering and XPS

analysis for Cu-2p3/2, Zn-2p3/2 and Sn-3d5/3 peaks were alternatively performed to investigate composition variations with depth. This reference film has overall Cu/(Cu+Zn+Sn) (abbreviated as Cu*), Zn/(Cu+Zn+Sn) (abbreviated as Zn*), and Sn/(Cu+Zn+Sn) (abbreviated as Sn*) values of 43.6%, 32.0%, and 24.4. This composition, slightly Cu-poor, Zn-rich, and Sn-poor compared to stoichiometric kesterite (with Cu*, Zn*, and Sn* values of 50%, 25%, and 25%, respectively), has been adopted by most of kesterite solar cells in the literature and produces better device performance than those with stoichiometric composition.[16,30] Studies by first-principle calculation suggested that this composition is favorable because such a growth condition may suppress the formation of undesired Cu-rich and Sn-rich defects, such as Cu_{Sn} and Sn_{Zn},[14] and encourage the formation of beneficial acceptors such as V_{Cu}.[31] Figure 2a shows the composition profile near the surface (∼300 nm) of the film measured by XPS along with the bulk composition measured by X-ray fluorescence (XRF). The detailed composition, measured by XRF and XPS, across the film from surface to the bottom is listed in Table 1. A full depth profile of the film from the top to the bottom is shown in the Supporting Information. It is shown that the surface is Sn-rich/Cu-poor/Zn-neutral relative to bulk composition. (Cu/(Cu+Zn+Sn) = 26.5% vs 43.6% for bulk; Zn/(Cu+Zn+Sn) = 34.9% vs 32.0% for bulk; Sn/(Cu+Zn+Sn) = 38.6% vs 24.4% for bulk) This result is consistent with some previous work,[32] but not all,[33] indicating that surface composition of kesterite thin films is highly processing dependent. Since the Sn ratio is as much as 1.5 times of the stoichiometric ratio of the bulk kesterite phase, the excess Sn could exhibit as one of the two possible forms, either Sn-rich secondary phases or point defects such as antisites or adatoms.
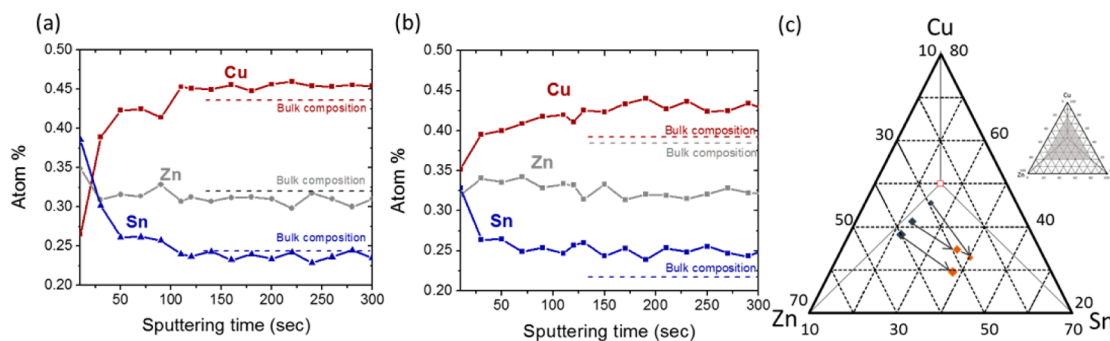
Figure 2. Composition depth profiles on the surface 300 nm of (a) the reference film and (b) the high-Zn film. (c) Ternary composition diagram of the initial bulk compositions (shown in blue) and the selenized surface compositions (shown in orange).

TABLE 1. Spatial Composition Distribution of the Selenized Films: The Reference and High Zn Samples[a]

method	bulk composition (Cu/Zn/Sn) XRF	surface composition (Cu/Zn/Sn) XPS	large grains (Cu/Zn/Sn) XPS	fine grains/MoSe$_2$ (Cu/Zn/Sn) XPS
reference	43.6%/32.0%/24.4%	26.5%/34.9%/38.6%	43.8%/32.1%/24.1%	43.6%/32.4%/24.0%
high Zn	38.6%/39.4%/22.0%	35.2%/32.0%/32.8%	41.6%/35.0%/23.4%	37.1%/42.2%/20.7%

[a] The bulk composition is obtained by XRF; the surface composition is obtained by XPS surface measurement; the large-grain and fine-grain/MoSe2 compositions are obtained by averaging the composition from the corresponding regions in the depth profile.

To further examine the existence of the excessive Sn species, XRD measurement is used, which is highly sensitive to the existence of SnSe and SnSe$_2$ even to extremely small quantity on the surface.[34] Figure S5 (Supporting Information) shows the absence of SnSe and SnSe$_2$ characteristic peaks in XRD, which diminishes the possibility of the formation of SnSe and SnSe$_2$ phases. Other Sn-based secondary phases, for example, Cu$_2$SnSe$_3$ and other Cu−Sn−Se phases, are also Cu-based and therefore can be excluded since the Cu is deficient in this case. This suggests that excess Sn near the surface most likely displays in the form of point defects such as Sn$_{Zn}$[14] and/or constitutes energy favorable surface reconstruction such as Sn adatoms and Sn$_{Zn}$.[35] It is consistent with the suggestion of first-principle studies[14,35] that the Sn-rich surface reconstruction composed by Sn$_{Zn}$ or Sn adatoms have relatively low surface energy compared to other types of surface reconstruction. The defects are likely formed in the high-temperature annealing process and frozen under a considerably fast cooling.[36,37] It is noteworthy that some of these Sn-excess defects are not simply structural defects but also electrical defects, acting as recombination centers for carriers as the density of states distribution is within the bulk bandgap of kesterite. Accordingly, suppressing the Sn excess and increasing the Zn excess on the film surface may reduce the interfacial recombination in the devices and achieve better device performance.

To suppress the Sn excess and increase Zn ratio on the film surface, we designed nanocrystal precursor with significantly higher Zn than the stoichiometric composition (Cu/(Cu+Zn+Sn), Zn/(Cu+Zn+Sn), and Sn/(Cu+Zn+Sn) as 38.63%, 39.43%, and 21.93%, respectively). The surface composition depth profile of the resulting selenized film is shown in Figure 2b, and the entire film depth profile is shown in Supporting Information Figure S6. The composition for the surface, large grain, and small grain of the high Zn film is also listed in Table 1. It is worth noticing that although the two films are prepared by nanocrystals with significantly different levels of Zn composition, the resulting large grains in the front of the films have very similar composition as shown in the composition depth profiles in Figure 2a,b. The extra portion of the Zn in high-Zn film has been found in the fine-grained layer of the film (Supporting Information Figure S6). This observation indicates that the nanocrystal film is able to self-regulate the composition of the large grains during growth, in which only appropriate amounts of elements are allowed to diffuse upward to form CZTSSe large grains. However, although the large-grain composition is not changed by using high-Zn nanocrystals, the surface composition is obviously different. The surfaces Cu/(Cu+Zn+Sn), Zn/(Cu+Zn+Sn), and Sn/(Cu+Zn+Sn) for the high-Zn film are 35.2%, 32.0%, and 32.8% at the surface, respectively. Although in general the surface composition is still Sn-rich/Cu-poor/Zn-neutral compared to its bulk composition, it is much less dramatically Sn-rich compared to the reference case using a moderate-Zn-content precursor. The correlation between surface composition of the selenized film and the bulk composition of the precursor nanocrystal films is further illustrated in the ternary diagram shown
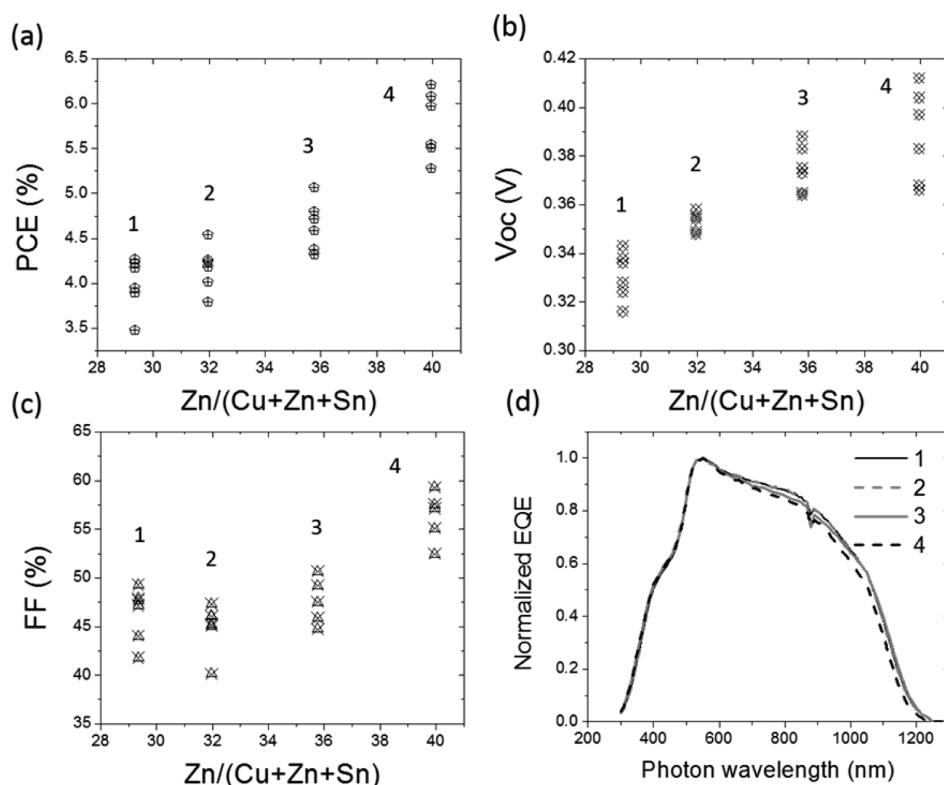
Figure 3. (a) Power conversion efficiency (total-area efficiency); (b) open-circuit voltage; (c) fill factor; and (d) normalized external quantum efficiency of four devices prepared from nanocrystal precursors with increasing Zn content. Zn/(Cu+Zn+Sn) ratios are 1−29.3%, 2−32.0%, 3−35.8%, and 4−40.0%.

in Figure 2c. According to the diagram, the surface composition of the films, compared with the bulk composition, is pushed toward Sn-rich direction, whereas through the introduction of much more Zn into the precursors, the Sn-rich surface composition can be partially corrected. This observation shows that the thermodynamically stable surface reconstruction is dependent on the chemical potential environment, that is, film composition during the growth, which is consistent with the findings in theoretical study.[35] It has been predicted that by growing the film under off-stoichiometric conditions toward Zn-rich Cu-poor, the surface energy of the surface constructed by Sn-enriched defects (like Sn_{Zn} and Sn adatoms) increases and becomes less thermodynamically favorable. The calculation may partially explain the fact that a relatively Zn-rich Cu-poor Sn-poor composition in precursor film leads to a higher Zn/Sn ratios in the surface of selenized film.

To evaluate the effect of surface composition on device performance, four devices with different bulk composition are fabricated. The bulk compositions of the kesterite films are shown in the ternary diagram in Supporting Information, Figure S7. The four films show increasing Zn/(Cu+Zn+Sn) ratios (29.3%, 32.0%, 35.8%, 40.0%) with fixed Cu/Sn ratio of 1.7−1.8. To be noted, Raman characterization shows that although the bulk compositions are different, all the films after

selenization exhibit the similar CZTSe phase, and no obvious secondary phases (Supporting Information Figure S8). A clear positive correlation has been found between the device performance and the composition (Figure 3a). By increasing the Zn/(Cu+Zn+Sn) from 29.3% to 40.0%, the cell efficiency has been increased from ∼4% to 6%. The major contribution of the improved J−V parameters is from the increased open-circuit voltages (V_{OC}) and fill factors (FF) (Figure 3b,c). Parasitic resistances including R_s and R_{sh} remain similar regardless of the different bulk compositions in the film. The above observation suggests that the cell efficiency is improved by the reduction of recombination loss rather than of optical or parasitic loss.

We further employ the external quantum efficiency (EQE) spectra to examine whether the recombination is associated with surface or bulk. As indicated by Figure 3d, the normalized EQE spectra of the four cells with different bulk composition are almost identical, which implies that the carrier collection in the bulk of the absorber is equally effective in all cases. It is likely that the bulk recombination rates are also similar in all cases. We thus suspect the improvement of inter-facial recombination rate may better explain the improvement of V_{OC} and FF. In addition, temperature-dependent studies on V_{OC} provide supportive evidence. Figure 4 shows the $V_{OC}−T$ plots of the four

devices. The data points extrapolate to recombination activation energies at 0 K. In most of the reported kesterite works, the activation energies obtained from this method is smaller than the band gap energy of the kesterite by a difference around or over 100 meV, which implies that the interfacial recombination rather than space-charge region recombination dominates the recombination processes. Our measurement here has also shown that the difference is around 100 meV for the better device made from a high-Zn film. The lower-efficiency devices, made from films with relatively lower Zn composition, have larger differences. The difference is as large as 200 meV for the two devices made from the lowest Zn bulk composition. This result indicates that by increasing the Zn composition in the growth environment, the interfacial recombination rate of the resulting devices is reduced. And since the occurrence of the reduced interfacial recombination also coincides with the occurrence of increased Zn/Sn ratios on the film surface, we therefore speculate that the suppression of Sn-excess surface defects has eased the interfacial recombination and improved the device performance.

When the surface composition is engineered via the use of high-Zn nanocrystal precursors (Cu*, Zn*, and Sn* = 39.2%, 38.4%, 22.4%, respectively), a best cell efficiency of 8.6% is obtained (active-area efficiency). The cells fabricated in identical conditions, achieved PCE ranging from 6.86% to 8.62% (Supporting Information, Table S1). These devices were fabricated by all-solution processing, which sequentially employed the spin-coating of CZTS nanocrystals and selenization of the resulting film, chemical-bath deposition of CdS buffer layer, and spin-coating of a silver nanowire and indium tin oxide (ITO) nanoparticle composite as the top electrode.[38] The current−voltage curve and the external quantum efficiency spectrum (EQE) of the device are shown in Figure 5a,b, respectively. Detailed electric parameters for the device were listed in Table 2, with V_{OC} of 0.435 V, J_{SC} of 32.5 mA/cm^2, and FF of 61.0%. A SEM cross-sectional image was shown in Figure 5c. As a comparison, a similar device using sputtered ITO as top electrode was also fabricated. The PCE, V_{oc}, J_{sc}, and FF. are 7.72% 0.431 mV, 28.4 mA/cm^2, and 63.2%, respectively, as shown in Table 2 (active-area efficiency), and the $J−V$ curve is also shown in Figure 5a. Compared with the device using sputtered ITO as top contact, the device based on AgNW-ITO composite has higher current partially because of the scattering-enhanced absorption by the nanowire networks, but a lower fill factor because of the higher resistance. The comparable performance of the all-solution processed devices to the vacuum-based processed ITO illustrates the potential of full solution processing in this material system.

We further examined and found that the device performance to this level of 8−9% efficiency is still limited by spatial distribution of the elements. The above results indicate that although the Sn-rich
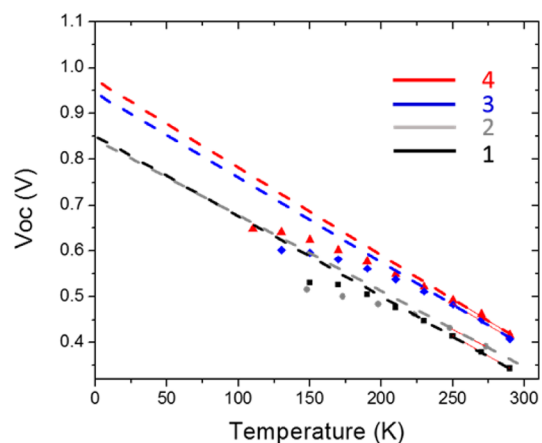

Figure 4. Temperature-dependent open-circuit voltages of the four devices described in Figure 3.

TABLE 2. Current−Voltage Parameters of the Best Cells by All-Solution Processing and Sputtering Deposited ITO

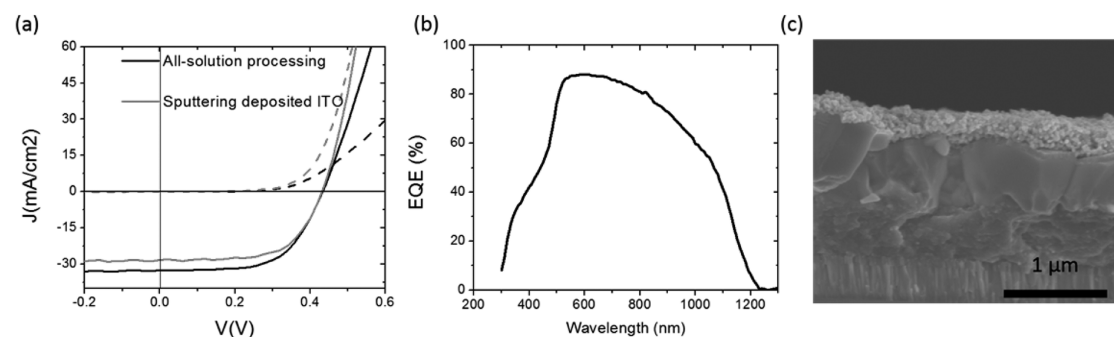| TCO	PCE (%)	V_{OC} (V)	J_{sc} (mA/cm^2)	FF (%)
Ag NWs composite	8.62	0.435	32.5	61.0
sputtering ITO	7.72	0.431	28.4	63.2

Figure 5. (a) The current−voltage characteristic of the best cells by all-solution processing and sputtering deposited ITO. (b) The external quantum efficiency (EQE) spectrum and the (c) cross-sectional SEM image of the best cell.
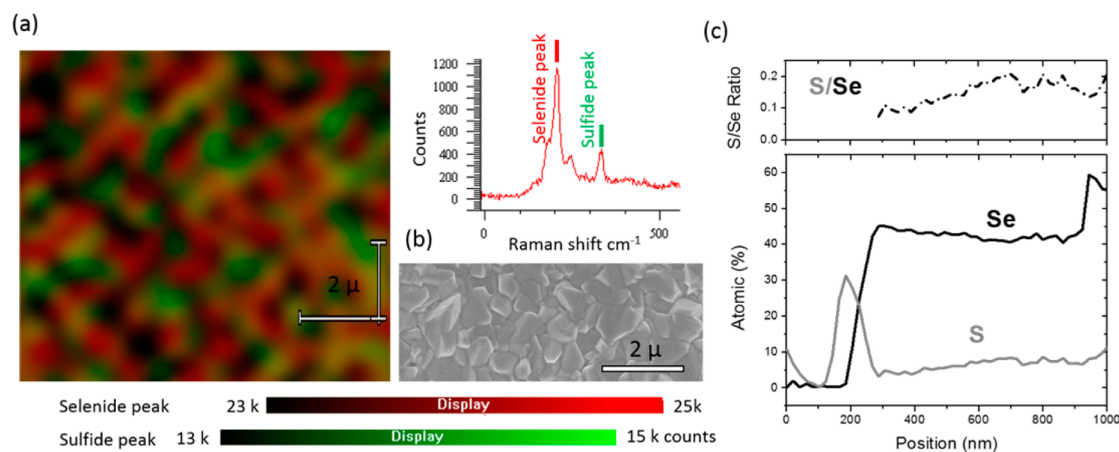
Figure 6. Raman spectra and intensity map of a typical selenized film. The peak at 201 cm^{-1} represents the selenide phase and its peak intensity is shown by red color in the map. The peak at 328 cm^{-1} represents the sulfide phase and its peak intensity is shown by green color. (b) SEM planar view of a typical selenized film. (c) S/Se variation in vertical direction across the film measured from EDS line scan by TEM.

surface has been largely suppressed, the surface still has a Zn/Sn ratio close to or less than 1, which likely still introduces a considerable amount of recombination paths in the vicinity of the junction. In addition to the vertical spatial distribution issue of the metals, the lateral/vertical distribution of chalcogen is also not ideal. A typical optimized CZTSSe film, which was later employed to produce over 7% device efficiency, was used to investigate the sulfur/selenium distribution by Raman scattering mapping. Figure 6a shows a blend of two intensity maps of different Raman peaks from a planar view of the film under 514 nm laser. The peak area of $Cu_2ZnSnSe_4$ characteristic peak at 201 cm^{-1} is displayed in red color by intensified brightness; the peak area of Cu_2ZnSnS_4 characteristic peak at 328 cm^{-1} is displayed in green color. As shown, the red patches and the green patches appear alternatively cross the film, which indicates the uneven distribution of sulfur and selenium. Interestingly, the mapping image shows a 500 nm distance between two patches in different color, which well matches the averaged grain size shown in SEM image. Therefore, the S/Se variation is probably attributed to the variation from grain to grain. Uneven S/Se lateral distribution inevitably produces uneven bandgap[28] distribution and limits the V_{OC} of the resulting device. The S/Se variation across the film in the vertical direction, which is measured from an EDS line scan by TEM, is shown in Figure 6c. Accordingly, the S/Se ratio increases toward the bottom of the films, which creates a considerable increase in bandgap and conduction band minimum (CBM) as well,[18] while, this uneven spatial distribution in the absorber could also be utilized to improve the device performance if controlled properly. The CBM gradients observed in CIGS solar cells are considered helpful for carrier collection because of the introduction of an additional electric field outside of the depletion region, guiding electrons to the right direction.[39,40] In brief, S/Se distributions both in the lateral and vertical directions warrant attention for either avoiding the irritating loss or further excelling the cell efficiency.

CONCLUSIONS

In summary, we have demonstrated spatial composition-dependent $Cu_2ZnSn(S,Se)_4$ device performance through the nanocrystal approach, and achieved 8.6% CZTS cell efficiency by full solution processing. XPS depth profiling has revealed the vertical redistribution of metallic elements within the selenized film fabricated from stoichiometric CZTS nanocrystals, producing an unfavorable Sn-rich composition at the top surface in the vicinity of the junction, compared to its inside bulk composition. Implications adopted from a first principle calculation suggest that the Sn-rich surface composition is likely due to the low energy of the Sn-excess defect-related surface reconstruction. By compensating the spatial composition deviation at the front surface through the use of the nanocrystals with high Zn/(Cu+Zn+Sn) ratio, we found a reproducible positive correlation between cell performance and Zn/(Cu+Zn+Sn) ratio in the as-deposited film. Optimized devices starting from CZTS nanocrystal ink with a Zn content 1.6 times more than that of the previously reported stoichiometry have resulted in higher power conversion efficiency. The best cell efficiency achieved is 8.6% through the full solution processing of Mo/CZTS/CdS/AgNWs-ITO nanoparticle layers. This compensation approach for spatial composition deviation through stoichiometric adjustments to nanocrystal precursors may also benefit other multielement photovoltaics, for example, I–V–VI$_2$, where film growth under chemical gradients is often required. Future efforts will attempt to deeply understand the underlying thermodynamic and

kinetic factors, and the ideal lateral/vertical composition distribution. High-efficiency inorganic photovoltaics will thus be enabled by the continuous advance on the rational engineering of elemental distributions.

EXPERIMENTAL METHODS

Synthesis of Nanocrystals. In a typical synthesis of CZTS nanocrystals, proportional amounts of copper acetylacetonate ($Cu(acac)_2$), zinc acetylacetonate hydrate ($Zn(acac)_2$), and tin(IV) bis(acetylacetonate) dichloride ($Sn(acac)_2Cl_2$) were mixed in 10 mL of oleylamine under vacuum from room temperature to 130 °C, and held at 130 °C for 30 min; then, the reaction was heated to 225 °C under Ar atmosphere, where 2 M of sulfur solution in 2 mL of oleylamine was injected at 225 °C, and the temperature was kept at 225 °C for 1 h. The reaction was cooled down to room temperature quickly, and the precipitated products were obtained by adding ethanol as precipitant. The dissolve/precipitation procedure was repeated one more time, and the nanocrystals were acquired and fully dispersed in a nonpolar solvent, such as toluene. The metal precursor ratio has been adjusted based on the device performance, and the optimized ratio for the metal precursors, appears to be 1.322, 1.223, 0.75 mmol of $Cu(acac)_2$, $Zn(acac)_2$, $Sn(acac)_2Cl_2$ respectively.

Absorber Layer Fabrication. To prepare the CZTSSe absorber layers, the nanocrystal inks were spin-coated in air on Mo-coated soda-lime glass. A soft baking at 300 °C for 2 min on a hot plate in air was applied after each spin-coating run. The thickness of the as-deposited film was adjusted to be 1.1 to 1.2 μm, by several spin-coating iterations. X-ray fluorescence (XRF) was used to check whether the CZTS film contains the desired composition prior to further fabrication. The following selenization was carried out at 560 °C for 20 min in a tube furnace, where the as-deposited films together with several hundred milligrams of selenium shot were put into a graphite box. The selenization temperature, the temperature ramping rate, the duration, and the argon base pressure can be varied. The optimized selenization conditions for the present CZTS films was carried out at 560 °C for 20 min, under high pressure (1.15 atm), with argon flow.

Device Fabrication. The typical procedure was as follows: First, molybdenum (Mo, around 350 nm) was deposited onto a Corning 2947 glass side by DC sputtering in argon. Then, the CZTS absorber layer was deposited according to the above procedure. Next, the cadmium sulfide (CdS) layer was deposited onto the CZTS layer by chemical bath deposition. Finally, AgNW/ITO-NP films were spin-coated onto the devices as a transparent top electrode. The total area of each cell is 0.12 cm². The effective area is measured carefully under optical microscope to calculate effective-area efficiency.

Characterization. The XRD patterns were collected on a PANalytical X'Pert Pro X-ray powder diffractometer using Cu Ka radiation (λ = 1.54050 Å). Bulk composition of the films was measured by X-ray fluorescence (XRF) calibrated by Rutherford backscattering spectrometry (RBS). Surface composition depth profiles were obtained from X-ray photoelectron spectroscopy (XPS). To ensure the results of XRF and XPS can be compared qualitatively, the sensitivity factors used for XPS are calibrated according to the result of XRF measurement of a film with uniform composition. The XPS measurements were performed using a Kratos XPS system. A monochromatic Al Kα (1486.6 eV) X-ray source was used for excitation. The SEM images were taken on Nova 230. TEM images were taken on an FEI CM 120 and T12 microscope operated at 120 kV, and HRTEM images were taken on an FEI Titan S/TEM microscope operated at 300 kV. Raman spectroscopy was performed on the films at room temperature using a Renishaw InVia model instrument with a 514.5 argon laser or 785 nm diode laser as a light source. Photovoltaic performance was characterized in air without any encapsulation under an AM1.5G filter at 100 mW/cm² using a Newport Oriel 92192 Solar Simulator, calibrated using a certified silicon photodiode. The EQE was measured using a system designed by Enli Tech.

REFERENCES AND NOTES

1. Tao, C. S.; Jiang, J.; Tao, M. Natural Resource Limitations to Terawatt-Scale Solar Cells. *Sol. Energy Mater. Sol. Cell.* **2011**, 3176–3180.
2. *Mineral Commodity Summaries 2011*; U.S. Geological Survey: Reston, VA, **2011**; p 198.
3. Wang, W.; Winkler, M. T.; Gunawan, O.; Gokmen, T.; Todorov, T. K.; Zhu, Y.; Mitzi, D. B. Device Characteristics of CZTSSe Thin-Film Solar Cells with 12.6% Efficiency. *Adv. Energy Mater.* **2014**, *4*, 1301465(1−5).
4. Repins, I.; Beall, C.; Vora, N.; DeHart, C.; Kuciauskas, D.; Dippo, P.; To, B.; Mann, J.; Hsu, W.-C.; Goodrich, A.; *et al.* Co-evaporated $Cu_2ZnSnSe_4$ Films and Devices. *Sol. Energy Mater. Sol. Cell.* **2012**, *101*, 154–159.
5. Shin, B.; Gunawan, O.; Zhu, Y.; Bojarczuk, N. A.; Chey, S. J.; Guha, S. Thin Film Solar Cell with 8.4% Power Conversion Efficiency Using an Earth-Abundant Cu_2ZnSnS_4 Absorber. *Prog. Photovolt: Res. Appl.* **2011**, *21*, 72–76.
6. Wu, W.; Cao, Y.; Caspar, J. V.; Guo, Q.; Johnson, L. K.; Malajovich, I.; Rosenfeld, H. D.; Choudhury, K. R. Studies of the Fine-Grain Sub-layer in the Printed CZTSSe Photovoltaic Devices. *J. Mater. Chem. C* **2014**, *2*, 3777–3781.
7. Hsu, W.; Repins, I.; Beall, C.; Dehart, C.; To, B.; Yang, W.; Yang, Y.; Noufi, R. Growth Mechanisms of Co-evaporated Kesterite: A Comparison of Cu-Rich and Zn-Rich Composition Paths. *Prog. Photovolt: Res. Appl.* **2014**, *22*, 35–43.
8. Hsu, W.-C.; Repins, I.; Beall, C.; DeHart, C.; Teeter, G.; To, B.; Yang, Y.; Noufi, R. The Effect of Zn Excess on Kesterite Solar Cells. *Sol. Energy Mater. Sol. Cell.* **2013**, *113*, 160–164.
9. Olekseyuk, I.; Olekseyuk, I. D.; Dudchak, P. L., IV Phase Equilibria in the $Cu_2S-ZnS-SnS_2$ System. *J. Alloys Compd.* **2004**, *368*, 135–143.
10. López-Marino, S.; Placidi, M.; Pérez-Tomás, A.; Llobet, J.; Izquierdo-Roca, V.; Fontané, X.; Fairbrother, A.; Espíndola-Rodríguez, M.; Sylla, D.; Pérez-Rodríguez, A.; *et al.* Inhibiting the Absorber/Mo-Back Contact Decomposition Reaction in $Cu_2ZnSnSe_4$ Solar Cells: The Role of a ZnO Intermediate Nanolayer. *J. Mater. Chem. A* **2013**, *1*, 8338.
11. Scragg, J. J.; Kubart, T.; Wa, J. T.; Ericson, T.; Linnarsson, M. K.; Platzer-bjo, C. Effects of Back Contact Instability on Cu_2ZnSnS_4 Devices and Processes. *Chem. Mater.* **2013**, *25*, 3162–3171.
12. Fairbrother, A.; García-Hemme, E.; Izquierdo-Roca, V.; Fontané, X.; Pulgarín-Agudelo, F. A.; Vigil-Galán, O.; Pérez-Rodríguez, A.; Saucedo, E. Development of a Selective Chemical Etch to Improve the Conversion Efficiency of Zn-Rich Cu_2ZnSnS_4 Solar Cells. *J. Am. Chem. Soc.* **2012**, *134*, 8018–8021.
13. Siebentritt, S.; Schorr, S. Kesterites—A Challenging Material for Solar Cells. *Prog. Photovolt: Res. Appl.* **2012**, *20*, 512–519.
14. Han, D.; Sun, Y. Y.; Bang, J.; Zhang, Y. Y.; Sun, H.-B.; Li, X.-B.; Zhang, S. B. Deep Electron Traps and Origin of P-type Conductivity in the Earth-Abundant Solar-Cell Material Cu_2ZnSnS_4. *Phys. Rev. B* **2013**, *87*, 155206 (1−5).

15. Chen, S.; Yang, J.; Gong, X.; Walsh, A.; Wei, S.-H. Intrinsic Point Defects and Complexes in the Quaternary Kesterite Semiconductor Cu$_2$ZnSnS$_4$. *Phys. Rev. B* **2010**, *81*, 35–37.

16. Katagiri, H.; Jimbo, K.; Tahara, M.; Araki, H.; Oishi, K. The Influence of the Composition Ratio on CZTS-based Thin Film Solar Cells. *Mater. Res. Soc. Symp. Proc.* **2009**, *1165*, M04–01.

17. Chen, S.; Gong, X.; Walsh, A.; Wei, S.-H. Electronic Structure and Stability of Quaternary Chalcogenide Semiconductors Derived from Cation Cross-Substitution of II-VI and I-III-VI2 Compounds. *Phys. Rev. B* **2009**, *79*, 1–10.

18. Chen, S.; Walsh, A.; Yang, J.-H.; Gong, X.; Sun, L.; Yang, P.-X.; Chu, J.-H.; Wei, S.-H. Compositional Dependence of Structural and Electronic Properties of Cu$_2$ZnSn(S,Se)$_4$ Alloys for Thin Film Solar Cells. *Phys. Rev. B* **2011**, *83*, 1–5.

19. Guo, Q.; Ford, G. M.; Yang, W.-C.; Walker, B. C.; Stach, E. a; Hillhouse, H. W.; Agrawal, R. Fabrication of 7.2% Efficient CZTSSe Solar Cells Using CZTS Nanocrystals. *J. Am. Chem. Soc.* **2010**, *132*, 17384–17386.

20. Leidholm, C.; Hotz, C.; Breeze, A.; Sunderland, C.; Ki, W.; Zehnder, D. *Final Report: Sintered CZTS Nanoparticle Solar Cells on Metal Foil*; NREL/SR-5200-56501; NREL: Golden, CO, **2012**.

21. Ford, G. M.; Guo, Q.; Agrawal, R.; Hillhouse, H. W. Earth Abundant Element Cu$_2$Zn(Sn$_{1-x}$Ge$_x$)S$_4$ Nanocrystals for Tunable Band Gap Solar Cells: 6.8% Efficient Device Fabrication. *Chem. Mater.* **2011**, *23*, 2626–2629.

22. Cao, Y.; Denny, M. S.; Caspar, J. V.; Farneth, W. E.; Guo, Q.; Ionkin, A. S.; Johnson, L. K.; Lu, M.; Malajovich, I.; Radu, D.; *et al*. High-efficiency Solution-Processed Cu$_2$ZnSn(S,Se)$_4$ Thin-Film Solar Cells Prepared from Binary and Ternary Nanoparticles. *J. Am. Chem. Soc.* **2012**, *134*, 15644–15647.

23. Zhou, H.; Song, T.-B.; Hsu, W.-C.; Luo, S.; Ye, S.; Duan, H.-S.; Hsu, C.-J.; Yang, W.; Yang, Y. Rational Defect Passivation of Cu$_2$ZnSn(S,Se)$_4$ Photovoltaics with Solution-Processed Cu$_2$ZnSnS$_4$:Na Nanocrystals. *J. Am. Chem. Soc.* **2013**, *135*, 15998–16001.

24. Mitzi, D. B.; Gunawan, O.; Todorov, T. K.; Barkhouse, D. A. R. Prospects and Performance Limitations for Cu−Zn−Sn−S−Se Photovoltaic. *Technol. Philos. Trans. A* **2013**, *371*, 20110432.

25. Gunawan, O.; Todorov, T. K.; Mitzi, D. B. Loss Mechanisms in Hydrazine-Processed Cu$_2$ZnSn(Se,S)$_4$ Solar Cells. *Appl. Phys. Lett.* **2010**, *97*, 233506.

26. Guo, Q.; Hillhouse, H. W.; Agrawal, R. Synthesis of Cu$_2$ZnSnS$_4$ Nanocrystal Ink and Its Use for Solar Cells. *J. Am. Chem. Soc.* **2009**, *131*, 11672–11673.

27. Zhou, H.; Hsu, W.-C.; Duan, H.-S.; Bob, B.; Yang, W.; Song, T.-B.; Hsu, C.-J.; Yang, Y. CZTS Nanocrystals: A Promising Approach for Next Generation Thin Film Photovoltaics. *Energy Environ. Sci.* **2013**, *6*, 2822–2838.

28. Wu, W.; Cao, Y.; Caspar, J. V.; Guo, Q.; Johnson, L. K.; Malajovich, I.; Rosenfeld, H. D.; Choudhury, K. R. Studies of the Fine-Grain Sub-layer in the Printed CZTSSe Photovoltaic Devices. *J. Mater. Chem. C* **2014**, *2*, 3777–3781.

29. Zhou, H.; Duan, H.-S.; Yang, W.; Chen, Q.; Hsu, C.-J.; Hsu, W.-C.; Chen, C.-C.; Yang, Y. Facile Single-Component Precursor for Cu$_2$ZnSnS$_4$ with Enhanced Phase and Composition Controllability. *Energy Environ. Sci.* **2014**, *7*, 998–1005.

30. Mitzi, D. B.; Gunawan, O.; Todorov, T. K.; Wang, K.; Guha, S. The Path Towards a High-Performance Solution-Processed Kesterite Solar Cell. *Sol. Energy Mater. Sol. Cell* **2011**, *95*, 1421–1436.

31. Chen, S.; Gong, X. G.; Walsh, A.; Wei, S.-H. Crystal and Electronic Band Structure of Cu$_2$ZnSnX$_4$ (X = S and Se) Photovoltaic Absorbers: First-Principles Insights. *Appl. Phys. Lett.* **2009**, *94*, 041903.

32. Bär, M.; Schubert, B. -a.; Marsen, B.; Krause, S.; Pookpanratana, S.; Unold, T.; Weinhardt, L.; Heske, C.; Schock, H.-W. Native Oxidation and Cu-Poor Surface Structure of Thin Film Cu$_2$ZnSnS$_4$ Solar Cell Absorbers. *Appl. Phys. Lett.* **2011**, *99*, 112103.

33. Repins, I.; Vora, N.; Beall, C.; Wei, S.; Yan, Y.; Romero, M.; Teeter, G.; Du, H.; To, B.; Young, M.; *et al*. Kesterites and Chalcopyrites: A Comparison of Close Cousins. *Mater. Res. Soc. Symp. Proc.* **2011**, *1324*, 97–108.

34. Vora, N.; Blackburn, J.; Repins, I.; Beall, C.; To, B.; Pankow, J.; Teeter, G.; Young, M.; Noufi, R. Phase Identification and Control of Thin Films Deposited by Co-evaporation of Elemental Cu, Zn, Sn, and Se. *J. Vac. Sci. Technol. A* **2012**, *30*, 051201.

35. Xu, P.; Chen, S.; Huang, B.; Xiang, H. J.; Gong, X.-G.; Wei, S.-H. Stability and Electronic Structure of Cu$_2$ZnSnS$_4$ Surfaces: First-Principles Study. *Phys. Rev. B* **2013**, *88*, 045427.

36. Schorr, S. The Crystal Structure of Kesterite Type Compounds: A Neutron and X-ray Diffraction Study. *Sol. Energy Mater. Solar C* **2011**, *95*, 1482–1488.

37. Scragg, J. J. S.; Choubrac, L.; Lafond, A.; Ericson, T.; Platzer-Björkman, C. A. Low-Temperature Order−Disorder Transition in Cu$_2$ZnSnS$_4$ Thin Films. *Appl. Phys. Lett.* **2014**, *104*, 041911.

38. Chung, C.-H.; Song, T.-B.; Bob, B.; Zhu, R.; Duan, H.-S.; Yang, Y. Silver Nanowire Composite Window Layers for Fully Solution-Deposited Thin-Film Photovoltaic Devices. *Adv. Mater.* **2012**, *24*, 5499–5504.

39. Dullweber, T.; Lundberg, O.; Malmstrom, J.; Bodegard, M.; Stolt, L.; Rau, U.; Schock, H. W.; Werner, J. H. Back Surface Band Gap Gradings in Cu(In,Ga)Se$_2$ Solar Cells. *Thin Solid Films* **2001**, *387*, 11–13.

40. Lundberg, O.; Bodegard, M.; Malmstrom, J.; Stolt, L. Influence of the Cu(In,Ga)Se$_2$ Thickness and Ga Grading on Solar Cell Performance. *Prog. Photovoltaics Res. Appl.* **2003**, *11*, 77.

ARTICLE